

On the Extraction of Microseismic Ground Motion from Analog Seismograms for the Validation of Ocean-Climate Models

Thomas Lecocq^{*1}, Fabrice Arduin², Fabienne Collin¹, and Thierry Camelbeeck¹

Abstract

We report on a pilot demonstration of the usefulness of analog seismograms to improve the database of ocean storms before the 1980s by providing additional data for the quantitative validation of ocean wave modeling, in particular for extreme events. We present a method for automatic digitization of paper seismograms to extract microseismic ground-motion periods and amplitudes. Each minute of the original paper records is scanned and vectorized. The amplitudes are calibrated based on the original metadata taken from official bulletins. The digitized time series is processed to extract power spectral densities, which are compared with modeled microseisms levels computed using a numerical ocean wave model. As a case study, we focus on one month of data recorded at the Royal Observatory of Belgium (ROB) from January to February 1953, around the “Big Flood” event, a tragic storm surge that flooded the lowlands of England, the Netherlands, and Belgium on 1 February 1953. The reconstructed spectrograms for the three components of ground motion show clear storm signatures that we relate to specific sources in the North Atlantic Ocean. However, our models of the Big Flood event based on these data do not result in the expected amplitudes as modeled compared to the observational data when the storm reached its maximum in the southern North Sea. We suggest that the source of microseisms recorded at ROB is related to the primary microseism generated in the North Sea, at periods of 7–8 s. Other discrepancies identified suggest small modifications of the source locations or energy. Reconstructed horizontal and vertical ground motions are coherent. This is a good news for the purpose of present-day analyses of constructing twentieth century ocean-climate models, especially as during much of that time only horizontal seismographs were installed at observatories.

Cite this article as Lecocq, T., F. Arduin, F. Collin, and T. Camelbeeck (2020). On the Extraction of Microseismic Ground Motion from Analog Seismograms for the Validation of Ocean-Climate Models, *Seismol. Res. Lett.* **91**, 1518–1530, doi: [10.1785/0220190276](https://doi.org/10.1785/0220190276).

Introduction

Seismologists observed and recorded the Earth’s continuous ground motions long before the onset of digital seismography, as early as 1855 (Shearer, 2019). At some locations, analog seismic data were recorded on smoked paper, with ink (e.g., drum recorded), or on photographic paper into the 1980s. For ocean waves, visual observations from ships make up nearly all the available data until 1946 with only a few instrumented records, which only became more common in the 1980s with the deployment of buoys (e.g., Gilhousen, 1987; Meindl and Hamilton, 1992). Global measurements of major ocean storms using wave heights became ubiquitous as of 1993 with satellite measurements (Davis, 2007), but coverage is usually not sufficient to record the peak of storms, and our general knowledge of the ocean wave climate therefore heavily relies on numerical models based on wind parameters obtained from atmospheric reanalyses (Rasclé and Arduin, 2013; Reguero *et al.*, 2019).

Because the wind speed and direction at sea level are diagnostic variables with few measurements before 1994, these estimates and their climatic trends are prone to artificial biases.

Another source of quantitative data comes from the microseisms recorded by seismometers (Bernard, 1990). Microseisms have been extensively studied since the early days of seismology (for a review see Ebeling, 2012, and references therein) mostly because of their presence in all seismic records. A microseism is defined as continuous ground motion arising from the interaction between the atmosphere, the oceans, and the solid Earth through energy transfer via the water column

1. Seismology–Gravimetry, Royal Observatory of Belgium, Brussels, Belgium;
2. University of Brest, CNRS, IRD, Ifremer, Laboratoire d’Océanographie Physique et Spatiale (LOPS), IUEM, Brest, France
*Corresponding author: thomas.lecocq@seismology.be
© Seismological Society of America

(for a complete review, see [Nakata et al., 2019](#), and references therein). Seismic records have been used to study the regional distribution of microseism sources, for example, by [Donn and Blaik \(1953\)](#) who used a simple tripartite azimuth computation to study the 1950 storm season in the northern Atlantic, or by [Friedrich et al. \(1998\)](#) using the first digital records of the Gräfenberg Array, Germany ([Harjes and Seidl, 1978](#)), to locate multiple sources of microseisms in the North Atlantic Ocean. Seismic data were also compiled by [Aster et al. \(2008, 2010\)](#) for studying the long-term evolution of microseism power based on all available digital data from the Seismic Research Observatory, the High-Gain Long Period and Global Seismic Network ([Albuquerque Seismological Laboratory \(ASL\)/USGS, 1972, 1974, 1988](#)).

Using 40 yr of seismic records (1954–1998) from Hamburg, Germany, [Grevemeyer et al. \(2000\)](#) showed that measurements on historical seismic records are related to possible changes in the wave climate in the northeast Atlantic Ocean. Similarly, [Dahm et al. \(2005\)](#) used historical seismic data from different locations in Europe and showed a good correlation between them for specific storm periods. Recently, [Gualtieri et al. \(2018\)](#) showed that tropical cyclones can be tracked using the spectral content of the microseisms generated by them, and that their intensity can be derived from the spectral amplitude of the short-period secondary microseism. [Hanafin et al. \(2012\)](#) showed that very long-period microseisms (above 9 s) are proportional to long ocean wave periods (twice the seismic period, over 18 s) and considered them to be fingerprints of extreme ocean storms.

The magnitude of microseisms is not simply related to the height of ocean waves (e.g., [Obrebski et al., 2012](#)). It is therefore necessary to transform a modeled wave climate into microseismic amplitudes as applied by [Stutzmann et al. \(2012\)](#) to validate a global microseismic model. [Stopa et al. \(2019\)](#) utilized a similar model for improving wave hindcasts by modifying the wind field in time and space, transforming wind to waves, and waves to microseisms that can be compared with seismic records. Here, we propose a new seismic digitization method, processing scanned paper seismograms from the analog instrumental epoch to extract microseism amplitude and frequency content (spectra). Those spectra, properly referenced in time and amplitude, are then compared with a microseism generation model based on the WAVEWATCH III wave model ([Tolman and the WAVEWATCH III Development Group, 2014](#)). For this pilot project, we will focus on the “Big Flood” of 1953, a massive storm surge event that dramatically flooded lowlands of the Netherlands, Belgium, and England and caused 2165 fatalities.

Seismic Analog Records

The first seismic records made at the Uccle station (UCC) of the Royal Observatory of Belgium (ROB) date back to 1898 ([Royal Observatory of Belgium, 1985](#); [Van Camp and Camelbeek, 2004](#)) and were acquired using a von Rebeur-

Ehlert triple horizontal pendulum built by Bosch (Strasbourg, France). At the beginning of the twentieth century, the ROB owned two Wiechert seismometers: one 1000 kg horizontal (installed in 1910, decommissioned in the 1970s) and one 1300 kg vertical (1911–1970s) seismometer, two Galitzin double-pendulum horizontal seismometers (1911–1914 and 1919–1962) and one Galitzin-Wilip vertical seismometer (1930–1970s). This Galitzin-Wilip seismometer was difficult to stabilize and its records were unreliable, making it essentially useless between 1930 and 1935 ([Somville, 1930, 1931, 1932, 1933, 1934, 1935](#)) until it was heavily modified by Somville in 1936 ([Somville, 1936, 1937a,b](#)) to be stable at different periods while ensuring that damping and recording remained identical to the original Galitzin-Wilip. Because of its modifications, we call this new instrument as the Galitzin-Wilip-Somville seismometer.

The Wiechert seismometers used a pen to scratch rolls of smoked paper as recorder, whereas Galitzin seismometers used a galvanometric system to direct a beam of light onto photographic paper. The advantage of the photo records over smoked paper is that the photo records generally have greater contrast between the trace and the background, which could be grayish or scratched on smoked paper. The friction of the pen on paper also altered the quality of the records, although this effect was more important for large amplitude resulting from seismic events than for microseisms.

The timing of seismic records is, by nature, critical. The recording systems at the ROB were synchronized with the “Bureau de l’Heure” (the “Time Office”) operated by the ROB in a close-by building. The timing accuracy was 1 s in 1909 and 0.1 s as of 1913 ([Somville, 1914](#), p. 176). The reference clocks, named “fundamentals,” were four Rieffler pendulums installed in a temperature-controlled basement until 1955 when the first quartz clocks were installed. The relative time encoding on paper seismograms is generally done by one of the three following ways: (1) a gap of one or more seconds at the end of each minute, generated by lifting the needle off the smoked paper or by intercepting the light beam to photographic paper; (2) a spike; or (3) a translation of a few millimeters of the trace. Our Galitzin records are of type (1): the photographic records show one second gaps at the end of every minute. The absolute time encoding is done by interrupting the light beam for 1 s every hour, allowing the measure of the time correction to add to the beginning of every minute.

The ROB still owns most of the analog records, either in paper form stored in one single wooden box per year of data, or digitized on microfilm (which records could also be scanned in the future, depending on the quality of preservation).

Digitizing Paper Seismograms and Extracting Ground Motion

Extracting digital seismic traces from scans (images) has been the subject of numerous articles in the past 20 yr and the

digitizing process can be classified either manually by clicking on all the wiggles of a seismic trace (e.g., Bromirski and Chuang, 2003; Pintore *et al.*, 2005), or automatically using image processing techniques to extract the wiggles (e.g., Baskoutas *et al.*, 2000; Church *et al.*, 2013; Wang *et al.*, 2014). Bromirski and Chuang (2003) show an example on their website (see [Data and Resources](#)) of scanned seismograms from a Galitzin-Wilip vertical seismometer for January 1941 and highlight its similarity with spectrograms that can be obtained nowadays with modern digital seismic data. The semi-automatic DigitSeis digitization software (Bogiatzis and Ishii, 2016) includes the automatic detection and digitization of seismic traces and timing marks while allowing manual corrections and adjustments from the user.

Our method is comparable to the one described in Wang *et al.* (2014) and is composed of the following steps, with changes to the methodology as developed in this study marked with an asterisk: scan, color inversion, thresholding*, binarization, rotation*, region “labeling,”* line thinning–skeletonization and ObsPy Trace object creation*. These steps are described in the following section. The digitization algorithm is written in Python, makes use of state of the art Python modules, and is available as Jupyter notebooks (see [Data and Resources](#)).

Scanning paper seismograms

The scanning of paper seismograms is time consuming and tedious but essential for the conservation of our archives (Okal, 2015). Until recently, ROB scans were restricted to significant event records. For this study, seismograms were scanned using a context HD ultra scanner capable of ingesting an 841 mm wide sheet of paper (width of an A0 ISO 216 standard). Such a scanner supports scanning photographic paper, but not smoked paper due to potential damage from the scanner drive rollers. The final image is saved to TIFF file format. For consistency, we used naming conventions with station name (e.g., UCC), seismometer orientation (vertical, north–south, or east–west), and the date of the record. For processing microseisms records, a resolution of 300 dpi is sufficient and is less computationally expensive during the processing than 1200 dpi, that is, the maximal resolution of the scanner.

Color inversion, thresholding, binarization, and rotation

Smoked paper seismograms have a black background (the smoke) and whitish traces, scratched by the pen, whereas developed photographic papers have a white background and a black trace. To easily identify both kinds of traces using the same algorithm, the photographic images are photo-inverted to obtain white traces. A threshold (Otsu, 1979) is applied to the image to reject small under-represented tones from the image. Finally, the image is binarized, that is, all positive values (traces) are set to 1 and the background to 0.

Next, we rotate the image to adjust for slight misalignment of the sheet in the scanner. This step is done using a Hough transform (Hough, 1962; Duda and Hart, 1972), that is, a computer visualization technique to automatically identify straight lines in an image. We only compute the transform for angles in a $\pm 5^\circ$ range. The technique outputs identified lines, described by their location and angle. The image is then rotated by the median angle to horizontalize the traces.

Region labeling and skeletonization

The “labeling” operation consists of identifying regions of the image that are connected and form a shape, in our case, continuous chunks of seismic traces. The regions have (x, y) coordinates in the image space and can therefore be located and easily manipulated for further processing. This processing will only occur if the region identified is long and narrow, as we expect short and wide regions to contain bad data, glitches, handwriting, or other irrelevant information. The current version of the computer code developed here only works with nonoverlapping traces. This means that strong teleseismic events or calibration pulses will be ignored and skipped. Computer vision and machine learning techniques should be exploited in the future to overcome this limitation.

A process of line thinning is then required to reduce a 2D region of an image containing an object of random shape to a simple line. 2D objects can be defined by their “skeleton” or “central line.” In the case of seismic records, this skeleton will be centered in the white pixels of the trace. Once identified, each trace is stored together with its (x, y) coordinates on the image.

ObsPy trace creation

The identified seismic traces are analyzed using standard modern processing, carried out by creating one ObsPy trace object per trace. The (x, y) coordinates of the traces are used to sort them timewise, and the length of each trace is 59 s. To evaluate the sampling rate of each trace, we consider the median length of all traces identified on one sheet and compute the number of pixels per second (pps), which is the sampling rate. On most of our scans at 300 dpi, the trace length is 359 pixels or around 6.085 Hz. This corresponds to a movement of the light beam on the paper of 3 cm per minute. All traces are then linearly detrended, resampled (interpolated) to a common 8 Hz sampling rate using a Lanczos interpolation, tapered with a 0.5 s taper on both ends, and high-pass filtered above 0.08 Hz (12.5 s). The start time of each trace is computed from its (x, y) coordinates.

Instrument response correction

The functioning and the instrument response of the Galitzin seismometers are known and documented in the official Bulletins of the ROB (Somville, 1922a,b). Table 1 shows the parameters for the Galitzin seismometers as they were operated in 1953 (Somville, 1953). The calibration values for the

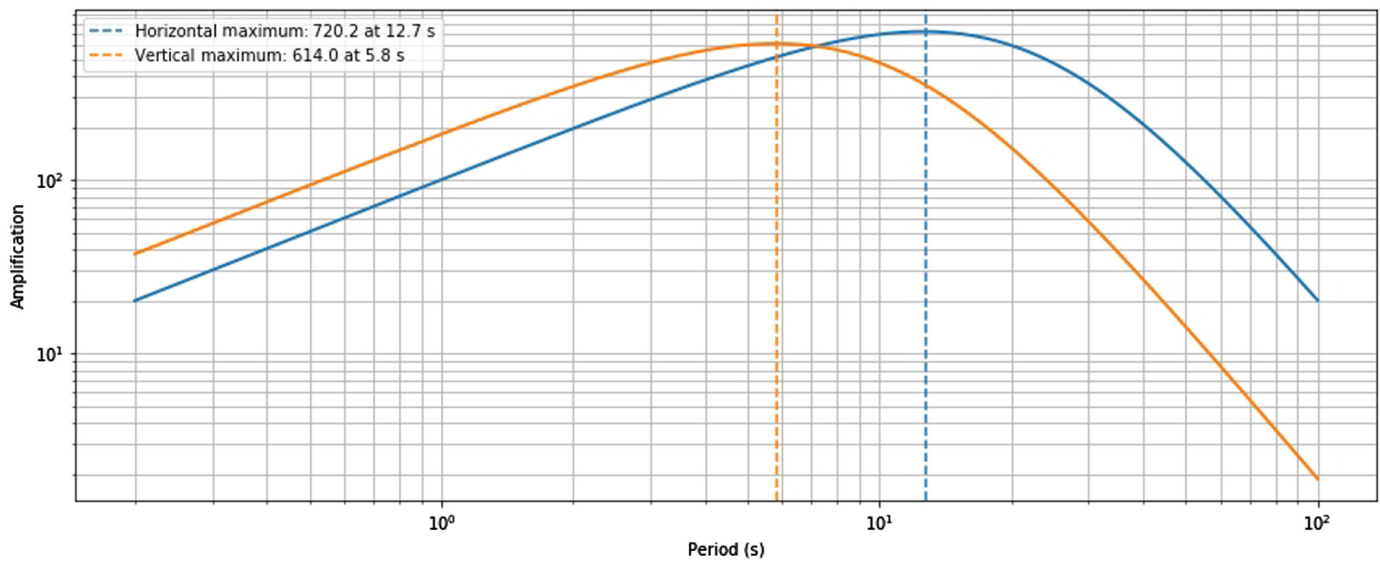


Figure 1. Amplitude response of the Galitzin seismometers owned by the Royal Observatory of Belgium (ROB) (Somville,

1930, 1937a, 1953). The color version of this figure is available only in the electronic edition.

transfer factor k are trusted for the horizontal unmodified pendulums. For the vertical, heavily modified instrument, we did not find any explanation on its determination but only its value in the reports from Somville (1937b). This vertical instrument has never been used to calculate the ground-motion amplitude (mentioned in the Bulletins) until it was decommissioned.

Using Table 1 and Galitzin’s formulations (Galitzin, 1911, pp. 107–108), we can recompute the real ground motion (x_m) from the measured amplitudes on the paper (y_m), that is, amplitude instrumental response for different periods (T_p):

$$x_m = C_1(1 + u_1^2)(1 + u^2)\sqrt{1 - \mu^2 f(u)}\frac{y_m}{T_p},$$

$$\text{with } C_1 = \frac{\pi l}{kA_1}, f(u) = \left[\frac{2u}{1 + u^2}\right]^2,$$

$$\text{and } u = \frac{T_p}{T}, u_1 = \frac{T_p}{T_1}, \quad (1)$$

in which T is the period of the pendulum, T_1 is the period of the galvanometer, l is the reduced pendulum length, μ is the damping constant, A_1 is the distance of the drum from the galvanometer mirror, and k is the transfer factor (Galitzin, 1911, p. 103). This step evidenced that the k transfer factor for the Galitzin-Willip-Somville seismometer was not correct, because digitized seismic traces are systematically three times larger than on the horizontal components. It is expected that the amplitude of the ground motions from Rayleigh and Love waves should have a ratio of horizontal to vertical, $H/V \approx 1.0$ (Darbyshire, 1954; Juretzek and Hadziioannou, 2016). We therefore empirically determined the k -factor to one-third of its value to scale the vertical traces to the trusted horizontal ones.

The amplitude response of the Galitzin seismometers (Fig. 1) can be utilized for studying microseisms because they have a maximal sensitivity in the primary (secondary) microseism band for the horizontal (vertical) Galitzin, respectively.

TABLE 1
1953 Parameters for the Galitzin Seismometers at ROB (Somville, 1953)

Instrument	T (s)	T_1 (s)	l (mm)	μ	A_1 (mm)	k
Galitzin east–west	21.5	21.8	123.8	+0.2	1040	38
Galitzin north–south	24.5	21.8	124.7	+0.2	1040	38
Galitzin-Willip-Somville Vertical	10.0	10.15	173.8	0.0	1060	290 (97)

ROB, Royal Observatory of Belgium; T , period of the pendulum; T_1 , period of the galvanometer; l , reduced pendulum length; μ , damping constant; A_1 , distance of the drum from the galvanometer mirror; k , transfer factor (Galitzin, 1911, p. 103). The two values for k for the vertical instrument are 290 from the bulletin (Somville, 1953) and the newly determined value, 97, based on the data (see the Instrument response correction section).

Since the very beginning of their usage, Galitzin seismometers were subject to criticisms about the nonvalidity of the assumption that the recorded data precisely reproduced the ground displacement (McComb and Wenner, 1936; Wenner and McComb, 1936). Because the eigenperiods of the Galitzin seismometer and galvanometer are the same, a slight phase difference between the true and recorded ground motions is incurred when the period of the recorded ground motion differs from the nominal seismometer period. The negative assessment was confirmed, and there is indeed a difference in phase between the two when the period of the recorded waves are larger or smaller than the nominal frequency. This discrepancy was also verified by Somville for the Galitzin-Willip vertical seismometer owned by the ROB. The phase shifts observed are orders of magnitude smaller than the studied period (0.1 s shift or less at 1.0 s). This instrumental shortcoming could have a strong impact on phase arrival-time measurements but is negligible for the study of microseism periods and amplitudes averaged over minutes to hours.

The dominant period of each one minute trace is extracted from its power spectral density (PSD, see the following section) and is used in equation (1) to obtain the amplification factor, that is, removing the instrument's amplitude response. The Galitzin seismometers and the digitizing technique have very little sensitivity to frequencies above 1 Hz.

PSD

The PSD of each seismic trace is computed using Welch's method (Welch, 1967). This method is known to reduce noise in the power spectra at the expense of reducing the frequency resolution because of frequency binning, which is efficient for obtaining information on the broad secondary microseismic peak.

The Welch method proceeds by splitting the signal in overlapping segments that are then windowed, in our case with a Hanning window (Blackman and Tukey, 1958), which more heavily weights the data at the center of the window. The windowed segments are then converted to a periodogram using the squared magnitude of the discrete Fourier transform. The resulting periodograms are averaged to reduce the variance of the power measurements.

The final product of our processing is three-hour medians of the individual, minute-long PSDs. This granularity was chosen to match the one used in the ocean modeling.

Ocean Microseism Generation Modeling

Our microseism model is a combination of a numerical wave model and a transformation of wave spectra into microseisms. The wave model is described in Rasle and Arduin (2013) and covers the world ocean, with a spatial resolution of 0.5° in longitude and latitude. The choice of parameterizations for the wind-wave generation and dissipation is particularly important

for the directional distribution of the wave energy and the resulting strength of microseism sources (Arduin *et al.*, 2011). It is forced by winds from the European Centre for Medium-Range Weather Forecasts' twentieth century reanalysis (Poli *et al.*, 2016). Based on satellite-derived wave heights for the year 2001, the wind-wave coupling coefficient β_{\max} was set to 1.7, giving a good representation of even the extreme wave heights (Stopa *et al.*, 2019). The wave model was run with and without shoreline reflection coefficient R for the wave energy.

The transformation of wave spectra to microseisms follows Arduin *et al.* (2011), with a summation of microseism sources along great circle paths and an attenuation with a constant Q coefficient. For UCC, we have used $Q = 200$ or $Q = 300$ and $R = 0.1$. The Q -values limit the range of the best fit obtained by Stopa *et al.* (2019) for seismic stations in continental Europe (180 for station ESK, Scotland, 220 for GRA, Germany, or 230 for SSB, France). The $R = 0.1$ is larger than traditionally used, but our objective here is to show first-order comparison and not to invert for R . Yet, for the years 2001–2014, these constant coefficients typically give a correlation coefficient $r = 0.95$ between the measured vertical ground displacement standard deviation over 3 hr and the modeled value of the same parameter, meaning that it is highly probable that the modeled events correspond to the synchronous ones observed at UCC. This processing predicts ground motions in a frequency band comparable to the band in which the Galitzin seismometer sensitivity is the greatest. Arduin *et al.* (2011) estimated that strong sources located at 1000 km away over a uniform $100 \times 100 \text{ km}^2$ area would induce a displacement variance of $1 \mu\text{m}^2$ when neglecting attenuation and seismic energy loss. Considering attenuation and ocean-solid earth coupling, the UCC station has its largest sensitivity in the first 1000 km around it and is sensitive to strong sources occurring up to 2000 km (Fig. 2). Looking at the spatial distribution of the modeled sources, we thus expect the UCC station to be sensitive to storms in the deep waters off the British Isles, the Norwegian coast, south of Iceland along the mid-Atlantic ridge, and the northwestern Mediterranean Sea.

Microseismic Activity in January–February 1953

At the end of January 1953, a storm formed in the North Atlantic Ocean (Fig. 2) and moved toward the northern tip of Scotland before changing direction to the southeast, in the North Sea toward the southern part of Denmark (Wemelsfelder, 1953; Wolf and Flather, 2005). While moving southeast in the North Sea, although its low-pressure center was not exceptionally deep, this storm generated strong winds and combined with high-spring tides, higher-than-usual sustained surge. During the night from 31 January to 1 February 1953, the surge height was maximal in the lowlands of England, the Netherlands, and Belgium. Extreme flooding

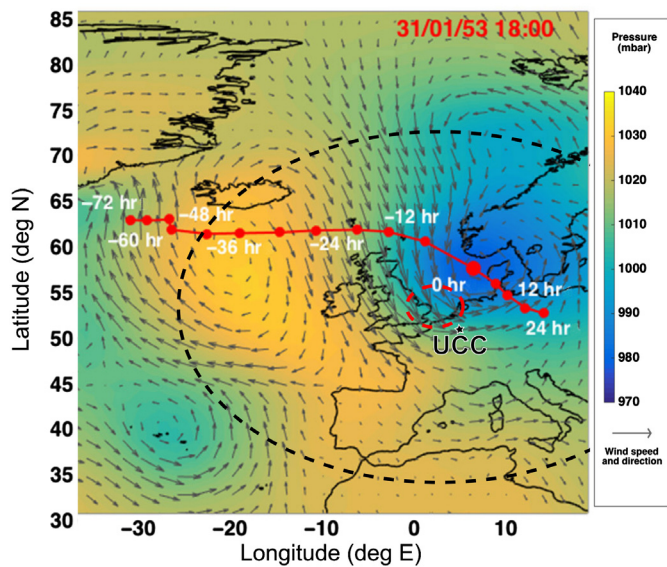


Figure 2. Map of the 1953 storm path 72 hr before until 24 after the Big Flood with the atmospheric pressure and wind fields 6 hr before the Big Flood, redrawn from [Wadey et al. \(2015\)](#). The dashed ellipses indicate the region where dramatic flooding occurred (red) and the area of maximal sensitivity (black, based on [Arduin et al., 2011](#)) for the Uccle (UCC) seismic station (black star). The color version of this figure is available only in the electronic edition.

due to dike failures led to a disastrous number of fatalities: 1836 in the Netherlands, 307 in the United Kingdom, and 22 in Belgium ([Gerritsen, 2005](#)). In the Netherlands, a total of 200,000 ha were flooded; 100,000 people were evacuated; 47,300 houses were damaged from which 9215 badly or irreparably ([Wemelsfelder, 1953](#)). This disaster, called “The Big Flood,” was at the impetus for the creation of the Delta Plan that today protects the Dutch lowlands from future surges ([Wemelsfelder, 1953](#)). In Belgium, between 1953 and 1977, more than 3.7 billion Belgian Francs (40 BEF = 1 EUR; 92 million Euros in 1977 Euros or, if corrected for inflation, 312 million Euros in 2019 Euros) were invested to repair and secure dikes and rivers within the Sigma Plan ([Ministère des Travaux Publics, 1977](#)). For this case study, we therefore decided to scan the records of the three components of the Galitzin seismometer between 15 January and 15 February 1953, centered on the “The Big Flood” event, and compare them to the modeled ground motion.

Despite a few records being incomplete or missing (sadly, the one containing the 1 February when the storm surge was maximal), the ground motion induced by this storm can still be extracted and PSDs reconstructed. One explanation for the absence of the records during the maximum of the storm is that the developed paper was unusable due to bad, probably clipped off-scale records. This hypothesis is supported by the records from the horizontal components, which exhibit

an extreme amplification of the traces on the mornings of 31 January and 2 February. Ninety analog seismograms (one month, three components) were systematically processed using the work flow as described earlier and provided the amplitude and the dominant period of each minute, together with the 3 hr PSDs of the ground motion recorded at UCC. Figure 3 shows the time evolution of the PSD—or spectrogram—of the microseisms records and of the model generated for the same period (Fig. 4). There are five periods of significant microseismic activity seemingly higher than a background level that could be estimated at $0.25 \mu\text{m}$: 17–21 January, 26–30 January, 31 January–2 February, 4–5 February, and finally 8–12 February.

Discussion

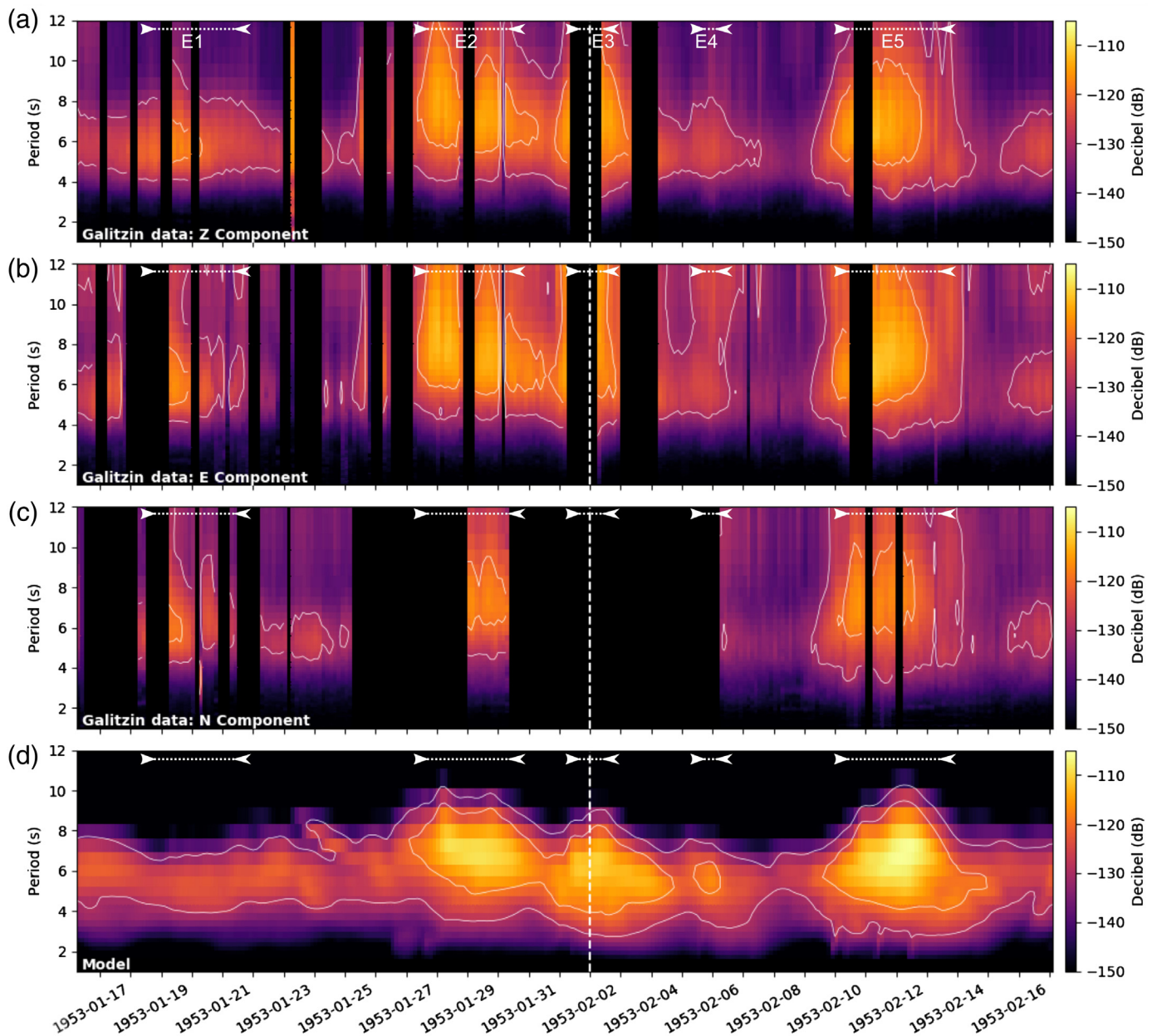
The microseismic activity recorded by the Galitzin and Galitzin-Wilip-Somville seismometers at station UCC shows strong changes during January–February 1953 (Fig. 3). The spectrograms for the three components are coherent, and we can therefore average the three spectrograms and take advantage of their slightly different time coverage or gaps. To compare the spectrograms with the modeled ground motion, we extract time series of the total amplitude of the ground motion (displacement δ_{rms}) and of the dominant period of the seismic waves from the observed and the modeled data (Fig. 5). Spectra (Fig. 3) are processed as in [Arduin et al. \(2011\)](#). The δ_{rms} of the microseisms is defined as the square root of the integral of the microseisms spectrum:

$$\delta_{\text{rms}} = \sqrt{\int_{0.08 \text{ Hz}}^{0.32 \text{ Hz}} F_{\delta} df_s},$$

with F_{δ} being the power spectrum of the ground displacement and f_s the frequency of the seismic wave.

There is a good agreement between the ground-motion amplitudes and dominant periods, except for the 17–21 January and the Big Flood event (24 January–2 February). Because of the original granularity of our data set, we also make use of the individual maximum ground motion per minute and compute their mean, median, and standard deviation values per 3 hr (Fig. 5). In the following, we discuss the different events of interest with respect to the modeled microseisms sources (Fig. 4).

The microseism source models do not reproduce the 17–21 January event (E1 on Figs. 3–5). The model (Fig. 4) locates sources close to the Azores, distributed sources between the Azores and the southern tip of Greenland and, at the same time, strong localized sources on the Norwegian coast and around the Shetland Islands. During this period, very strong sources are also located at the southern tip of Greenland. Changes of Q are not sufficient to significantly increase the effect of this storm, so we suggest that the two broad sources should have been more energetic than currently modeled.



For the 24–25 January event visible on the modeled data, there is a slight increase in amplitude, but the maximum is missed and could not be investigated due to a gap in the data.

The 26–30 January interval (E2) corresponds to sources illuminating the entire west coast of Europe, including south Iceland, the United Kingdom, and Ireland, together with a broad source in the Norwegian Sea (Fig. 4). The model predicts reduced ground-motion amplitudes with less variations than in the observed data. The strongest peak in the observed data corresponds to the arrival of the modeled seismic sources on the west coast of the United Kingdom and Ireland.

The Big Flood, the 31 January–2 February storm (E3) shows the largest discrepancy between the model and observations. During this period, the storm moved around the northern tip of Scotland and then progressed southward toward the English

Figure 3. 15 January–15 February 1953 displacement power spectral density (PSD) spectrograms based on the automatically extracted time series for the (a) vertical, (b) east–west, (c) north–south components, and (d) the result of the modeling using WAVEWATCH III and coastal reflections (REF102040). The thin white contours that highlight the -130 and -120 dB levels are indicated for illustration purposes only. The thick dashed white line indicates the time of occurrence of the Big Flood. The arrows indicate the five periods of significant microseismic activity; labeled E1–E5 in the [Microseismic Activity in January–February 1953](#) section and the following figures. The color version of this figure is available only in the electronic edition.

Channel. The highest peak in microseism amplitude and longest period microseisms are completely absent in the modeling. The difference between observed and predicted values is almost two-fold ($1 \mu\text{m}$) in amplitude and 1 s in period. The southern

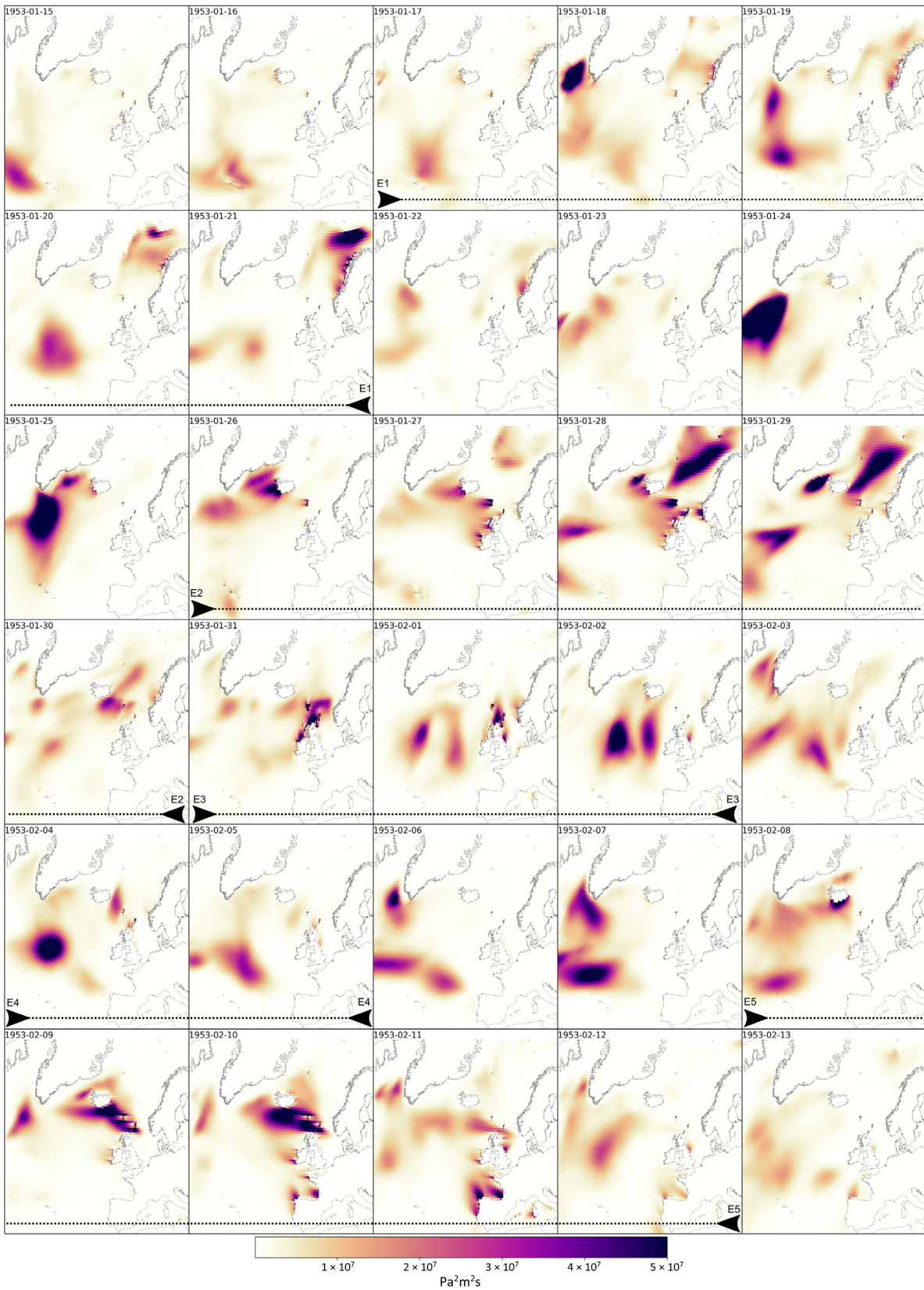
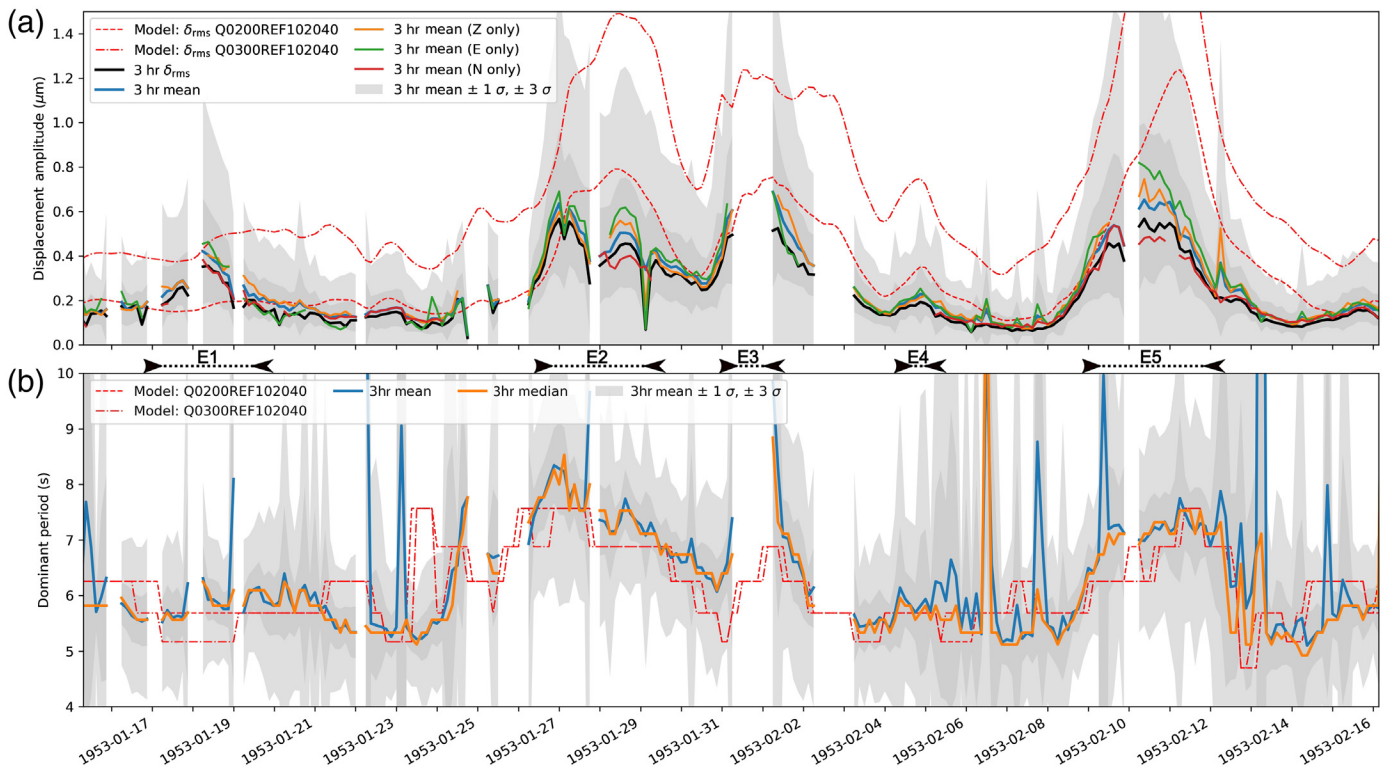


Figure 4. Modeled daily average microseismic sources obtained from ocean modeling: the PSD of equivalent surface pressure summed over all periods, not corrected for coupling (WAVEWATCH III and coastal reflections REF102040). The arrows indicate the five periods of significant microseismic activity. The

map extents are east–west: $-40, 15^\circ$, north–south: $35, 75^\circ$. The map projections Lambert conform (central latitude and longitude: 50.0° and 0.0°). The color version of this figure is available only in the electronic edition.



North Sea is characterized by shallow waters (10–150 m) with weak coupling between ocean waves and the ground and therefore should contribute only low-amplitude microseisms, which is what the model indeed predicts. The data, however, indicate that strong microseismic energy was recorded at the time of the storm. To resolve this discrepancy, we tried increasing the Q -factor from 300 to 400 for the area because we know from other seismic studies (Camelbeek, 1985; El Bouch *et al.*, 2002; Van Noten *et al.*, 2017; Mayor *et al.*, 2018) that the attenuation in northeast Belgium is low due to the presence of the west-northwest–east-southeast-extending Brabant–London massif, but the changes are too subtle to account for the nearly doubled amplitude difference. Another explanation could be that the modeled data only represent secondary microseisms, because there is recent evidence that short-period (5–8 s) primary microseisms could be generated in the North Sea (Becker *et al.*, 2019). This duality of generated microseisms would explain the strong energy measured, as well as the dominant period around 7–8 s, coherent with the work of Choi *et al.* (2018) who calculated the dominant sea wave periods to be between 7 and 9 s during the maximum of the storm. The study of primary microseism generation, specifically in the North Sea, has recently been addressed (Juretzek and Hadziioannou, 2017; Becker *et al.*, 2019) and should soon provide new modeling theories to compare with our results. The local wind field around UCC, also known as a source of seismic noise, for example, by its interaction with trees, can be ruled out, as most of the seismic energy radiated is at the first mode of resonance of trees, around 1–5 s maximum (Roux *et al.*, 2018), whereas higher modes occur at much higher frequency.

Figure 5. Comparison of the (a) ground displacement amplitude and its (b) dominant period for the modeled and observed data from digitized seismograms of the UCC station. Two ocean-generated ground-motion models with different Q -factor are presented. The arrows indicate the five periods of significant microseismic activity seemingly higher than a background level that could be estimated at $0.25 \mu\text{m}$: 17–21 January, 26–30 January, 31 January–2 February, 4–5 February, and finally 8–12 February. The color version of this figure is available only in the electronic edition.

The trends in recovered UCC microseism frequency content and amplitudes during the 4–5 February period (E4) are consistent with sources located in the center of the North Atlantic. The modeled amplitudes are slightly higher than the observations but the trends are similar. To match those, either Q should be lower (more attenuation) or the source should be farther away or weaker.

The trends during the 8–12 February interval (E5) are consistent with two sources located south of Iceland, moving south toward the west coasts of the United Kingdom and Ireland, then Brittany (France), Bay of Biscay (northeast Atlantic Ocean), Galicia (Spain), and the entire west coast of Spain and Portugal, ending with sources located on the west coast of Sardinia. The model exhibits similar amplitudes as the data, but with a +1 day lag with respect to the maximum of the 8–12 February storm. The maximum observed amplitudes occurred on 10 February, when the storm hit Scotland simultaneously with Galicia and the Bay of Biscay. There could also be parts of

the southern North Sea affected by stronger waves, and the explanation of the absence of the primary microseism above could also apply here.

Differences between observed and modeled ground motion could also arise from the uncertainties on the calibration parameters of the instruments. The response of horizontal Galitzin pendulums has been known and used during most of the century and is trusted. An error in the amplification factor would lead to a scalar multiplication factor between observed and modeled time series. An error in the shape of the amplitude–frequency response could explain differences, but our results show that periods of activity having the same dominant period exhibit different behaviours in terms of recovered ground motion (e.g., E1 vs. E4).

Conclusions

The digitization of analog seismograms allows reconstructing the evolution of the microseismic energy recorded at a single location. Because of its importance for locating earthquakes, the timing of the seismic records has always been the subject of great attention and is very accurate in UCC since 1913, which allows obtaining a high time resolution of observations. For each minute of digitized data, we are able to produce one PSD spectrum. Averaging them by hour or 3 hr, we can compare the seismic energy observations with modeled microseism obtained from the reanalysis of climate data, as done with WAVEWATCH III. Observations from a single seismometer correspond to the sum of pressure sources originating from a radius of a few thousand kilometers around the station, summing up along great circle paths and attenuating with distance. The observations have, therefore, a very high-temporal resolution while integrating spatially.

The analog seismic data were digitized to cover a one-month interval centered on the tragic Big Flood event that surged in the lowlands of the Netherlands, the United Kingdom, and Belgium, and it exhibits changes in ground displacement amplitude and period. Those trends can be directly linked to the behavior of specific sources in the North Atlantic Ocean, the Norwegian Sea, and the North Sea. Although trends in recovered and modeled microseism amplitude and period are similar, discrepancies between the two data sets raise questions. For the Big Flood event itself, the failure of the model to accurately reproduce the seismic energy recorded could be explained by a strong local source of primary microseism, not modeled here, with wave periods around 7–8 s. This effect could also explain the one-day difference in the maximum of the energy observed for the 8–12 February storm. These results suggest the necessity for additional research to provide a more precise combined model for primary and secondary microseism activity. The 4–5 February event also exhibits differences between observed and modeled data, and such events are particularly interesting as they are the most difficult to accurately model due to their remoteness from the shores and thus from

most land-based observations. The uncertainties on the instrument response could be a cause for differences between observed and modeled ground motions, but our results suggest that different periods of activity exhibit different amplitudes while sharing the dominant period, excluding at least partly an effect of the instrument. This should be verified by adding more data (years) or more identical instruments (from other locations) and compare with other instruments recording during the same time periods.

Our digitizing method is providing good results in the simple case of clear wiggles like the one recorded by the Galitzin seismometers. For more complex situations including overlaps, spikes, calibration pulses, etc., this method will fail. In that sense, solutions like the DigitSeis digitization software (Bogiatzis and Ishii, 2016) are much more evolved and promising. Including computer vision and machine learning for identifying the wiggles and their continuity could reduce the amount of human interaction needed in the digitization process.

We show that the amplitude and dominant period of the ground-motion displacement can be reconstructed independently using vertical or horizontal seismometers. This will facilitate the use of even earlier records, as horizontal seismographs were the first type of instruments installed worldwide. Analog seismic data from different observatories can therefore be used to add constraints on atmosphere–ocean–solid Earth couplings, to study different areas of the oceans and to better locate the microseismic sources, similar to the recent studies with digital seismic data. Merging analog and digital data would facilitate reanalyses over the entire twentieth century.

Data and Resources

Analog seismograms used in this article are the property of the Royal Observatory of Belgium (ROB) and can be consulted at any time upon request to the ROB. Scanned analog seismograms were processed using NumPy (Oliphant, 2006), SciPy (Virtanen *et al.*, 2020), Scikit-Image (van der Walt *et al.*, 2014), ObsPy (Beyreuther *et al.*, 2010; Krischer *et al.*, 2015), and Pandas (McKinney, 2012). Figures were created with Matplotlib (Hunter, 2007), and maps were plotted using Cartopy (Met Office, 2010). The modeled data from WAVEWATCH III are available from the FTP server of Ifremer: <ftp://ftp.ifremer.fr/ifremer/ww3/HINDCAST/SISMO> (last accessed September 2019). It comes in NetCDF format (Rew and Davis, 1990), which is read using the NetCDF4-python module (Whitaker *et al.*, 2019). The whole processing has been implemented in Jupyter notebooks (Kluyver *et al.*, 2016) and is accessible open and free on the authors' GitHub account (https://github.com/ThomasLecocq/SRL_2020_Historical, last accessed February 2020). Seismic digitizing software (SeisDig) is available at <http://iodlabs.ucsd.edu/peter/seismology/SeisDig.html> (last accessed September 2019).

Acknowledgments

C. Hadziioannou is acknowledged for the discussions about the primary microseism in the North Sea. C. Caudron, A. Watlet, and K. Van Noten are acknowledged for the discussions and for proofreading of

the article. Two anonymous reviewers and Editor-in-Chief Allison Bent are acknowledged for their comments and suggestions, which improved the quality of the article. This article has benefited greatly from Sharon K. Reamer's skilled copyediting. This article is the result of an idea that emerged from informal discussions at a summer school organized as part of the COST-Action TIDES "Time Dependent Seismology" (COST-ES1401). Baudouin Bukasa, Corentin Caudron and Sylvain Nowé are acknowledged for their help with the scanning of analog seismograms.

References

- Albuquerque Seismological Laboratory (ASL)/USGS (1972). High-gain long-period network, doi: [10.7914/SN/HG](https://doi.org/10.7914/SN/HG).
- Albuquerque Seismological Laboratory (ASL)/USGS (1974). Seismic research observatory, doi: [10.7914/SN/SR](https://doi.org/10.7914/SN/SR).
- Albuquerque Seismological Laboratory (ASL)/USGS (1988). Global seismograph network - IRIS/USGS, doi: [10.7914/SN/IU](https://doi.org/10.7914/SN/IU).
- Ardhuin, F., E. Stutzmann, M. Schimmel, and A. Mangeny (2011). Ocean wave sources of seismic noise, *J. Geophys. Res.* **116**, C09004, 1–21, doi: [10.1029/2011JC006952](https://doi.org/10.1029/2011JC006952).
- Aster, R. C., D. E. McNamara, and P. D. Bromirski (2008). Multidecadal climate-induced variability in microseisms, *Seismol. Res. Lett.* **79**, no. 2, 194–202.
- Aster, R. C., D. E. McNamara, and P. D. Bromirski (2010). Global trends in extremal microseism intensity, *Geophys. Res. Lett.* **37**, L14303, 1–5, doi: [10.1029/2010GL043472](https://doi.org/10.1029/2010GL043472).
- Baskoutas, I. G., I. S. Kalogeras, M. Kourouzidis, and G. Panopoulou (2000). A modern technique for the retrieval and processing of historical seismograms in Greece, *Nat. Hazards* **21**, 55–64.
- Becker, D., T. Kruse, F. Dethof, C. Weidle, and C. Hadziioannou (2019). Microseism in the North Sea: Tidal forcing, H/V-variability and a future monitoring network, *EGU General Assembly*, Vienna, Austria, 1 pp.
- Bernard, P. (1990). Historical sketch of microseisms from past to future, *Phys. Earth Planet. In.* **63**, nos. 3/4, 145–150.
- Beyreuther, M., R. Barsch, L. Krischer, T. Megies, Y. Behr, and J. Wassermann (2010). ObsPy: A Python toolbox for seismology, *Seismol. Res. Lett.* **81**, no. 3, 530–533.
- Blackman, R. B., and J. W. Tukey (1958). The measurement of power spectra from the point of view of communications engineering - Part I, *Bell Syst. Tech. J.* **37**, no. 1, 185–282.
- Bogiatzis, P., and M. Ishii (2016). DigitSeis: A new digitization software for analog seismograms, *Seismol. Res. Lett.* **87**, no. 3, 726–736.
- Bromirski, P. D., and S. Chuang (2003). SeisDig: Software to digitize scanned analog seismogram images, *User's Manual*, 28 pp., available at <https://escholarship.org/uc/item/76b2m74m> (last accessed March 2020).
- Camelbeek, T. (1985). Some notes concerning the seismicity in Belgium—Magnitude Scale—Detection capability of the Belgian seismological stations, in *Seismic Activity in Western Europe*, P. J. Melchior (Editor), Springer, Dordrecht, The Netherlands, 99–108.
- Choi, B. H., K. O. Kim, J.-H. Yuk, and H. S. Lee (2018). Simulation of the 1953 storm surge in the North Sea, *Ocean Dynam.* **68**, no. 12, 1759–1777.
- Church, E. D., A. H. Bartlett, and M. A. Jourabchi (2013). Raster-to-vector image analysis for fast digitization of historic seismograms, *Seismol. Res. Lett.* **84**, no. 3, 489–494.
- Dahm, T., F. Krüger, H.-H. Essen, and M. Hensch (2005). Historic microseismic data and their relation to the wave-climate in the North Atlantic, *Meteorologische Zeitschrift* **14**, no. 6, 771–779.
- Darbyshire, J. (1954). Structure of microseismic waves: Estimation of direction of approach by comparison of vertical and horizontal components, *Proc. Math. Phys. Sci.* **223**, no. 1152, 16.
- Davis, G. K. (2007). History of the NOAA satellite program, *J. Appl. Rem. Sens.* **1**, no. 1, 012504.
- Donn, W. L., and M. Blaik (1953). A study and evaluation of the tripartite seismic method of locating hurricanes, *Bull. Seismol. Soc. Am.* **43**, no. 4, 311–329.
- Duda, R. O., and P. E. Hart (1972). Use of the Hough transformation to detect lines and curves in pictures, *Commun. ACM* **15**, no. 1, 11–15.
- Ebeling, C. W. (2012). Chapter One - Inferring ocean storm characteristics from ambient seismic noise: A historical perspective, in *Advances in Geophysics*, R. Dmowska (Editor), Vol. 53, Elsevier, Amsterdam, The Netherlands, 1–33, doi: [10.1016/B978-0-12-380938-4.00001-X](https://doi.org/10.1016/B978-0-12-380938-4.00001-X).
- El Bouch, A., T. Camelbeek, and H. Martin (2002). Atténuation des ondes sismiques en Belgique et dans les régions limitrophes à partir de la coda des tremblements de terre locaux, *Geologica Belgica* **5**, nos. 1/2, 17–29 (in French).
- Friedrich, A., F. Krüger, and K. Klinge (1998). Ocean-generated microseismic noise located with the Gräfenberg array, *J. Seismol.* **2**, no. 1, 47–64.
- Galitzin, B. B. (1911). Ueber ein neues aperiodisches horizontalpendel mit galvanometrischer fernregistrierung, Buchdr. der K. Akademie der wissenschaften, St. Petersburg, Russia (in German).
- Gerritsen, H. (2005). What happened in 1953? The Big Flood in the Netherlands in retrospect, *Phil. Trans. Roy. Soc. London* **363**, no. 1831, 1271–1291.
- Gilhousen, D. B. (1987). A field evaluation of NDBC moored buoy winds, *J. Atmos. Oceanic Technol.* **4**, no. 1, 94–104.
- Grevemeyer, I., R. Herber, and H.-H. Essen (2000). Microseismological evidence for a changing wave climate in the northeast Atlantic Ocean, *Nature* **408**, no. 6810, 349–352.
- Gualtieri, L., S. J. Camargo, S. Pascale, F. M. E. Pons, and G. Ekström (2018). The persistent signature of tropical cyclones in ambient seismic noise, *Earth Planet. Sci. Lett.* **484**, 287–294.
- Hanafin, J. A., Y. Quilfen, F. Ardhuin, J. Sienkiewicz, P. Queffeuilou, M. Obrebski, B. Chapron, N. Reul, F. Collard, D. Corman, *et al.* (2012). Phenomenal sea states and swell from a North Atlantic storm in February 2011: A comprehensive analysis, *Bull. Am. Meteorol. Soc.* **93**, no. 12, 1825–1832.
- Harjes, H., and D. Seidl (1978). Digital recording and analysis of broad-band seismic data at Gräfenberg (GRF) Array, *J. Geophys.-Zeitschrift Fur Geophysik* **44**, no. 5, 511–523.
- Hough, P. V. C. (1962). Method and means for recognizing complex patterns, available at <https://patents.google.com/patent/US3069654/en> (last accessed March 2020).
- Hunter, J. (2007). Matplotlib: A 2d graphics environment, *Comput. Sci. Eng.* **9**, no. 3, 90–95.

- Juretzek, C., and C. Hadziioannou (2016). Where do ocean microseisms come from? A study of Love-to-Rayleigh wave ratios, *J. Geophys. Res.* **121**, no. 9, 6741–6756.
- Juretzek, C., and C. Hadziioannou (2017). Linking source region and ocean wave parameters with the observed primary microseismic noise, *Geophys. J. Int.* **211**, no. 3, 1640–1654.
- Kluyver, T., B. Ragan-Kelley, F. Pérez, B. E. Granger, M. Bussonnier, J. Frederic, K. Kelley, J. Hamrick, J. Grout, S. Corlay, *et al.* (2016). Jupyter notebooks - A publishing format for reproducible computational workflows, in *Positioning and Power in Academic Publishing: Players, Agents and Agendas*, F. Loizides and B. Schmidt (Editors), ELPUB, IOS Press, Amsterdam, The Netherlands, 87–90.
- Krischer, L., T. Megies, R. Barsch, M. Beyreuther, T. Lecocq, C. Caudron, and J. Wassermann (2015). ObsPy: A bridge for seismology into the scientific Python ecosystem, *Comput. Sci. Discov.* **8**, no. 1, 014003, 1–17.
- Mayor, J., P. Traversa, M. Calvet, and L. Margerin (2018). Tomography of crustal seismic attenuation in metropolitan France: Implications for seismicity analysis, *Bull. Earthq. Eng.* **16**, no. 6, 2195–2210.
- McComb, H. E., and F. Wenner (1936). Shaking-table investigations of teleseismic seismometers, *Bull. Seismol. Soc. Am.* **26**, no. 4, 26.
- McKinney, W. (2012). *Python for Data Analysis: Data Wrangling with Pandas, NumPy, and IPython*, O'Reilly Media, Inc, Sebastopol, California.
- Meindl, E. A., and G. D. Hamilton (1992). Programs of the national data buoy center, *Bull. Am. Meteorol. Soc.* **73**, no. 7, 985–994.
- Met Office (2010). *Cartopy: A Cartographic Python Library with A Matplotlib Interface*, Met Office, Exeter, United Kingdom, available at <http://scitools.org.uk/cartopy> (last accessed March 2020).
- Ministère des Travaux Publics (1977). Plan Sigma pour la protection du bassin de l'Escaut Maritime contre les marées-tempêtes de la mer du nord, *Technical Rept.*, Ministère des Travaux Publics (in French).
- Nakata, N., L. Gualtieri, and A. Fichtner (2019). *Seismic Ambient Noise*, Cambridge University Press, Cambridge, United Kingdom.
- Obrebski, M., F. Arduin, E. Stutzmann, and M. Schimmel (2012). How moderate sea states can generate loud seismic noise in the deep ocean, *Geophys. Res. Lett.* **39**, L11601, 1–6, doi: [10.1029/2012GL051896](https://doi.org/10.1029/2012GL051896).
- Okal, E. A. (2015). Historical seismograms: Preserving an endangered species, *GeoResJ* **6**, 53–64.
- Oliphant, T. E. (2006). *Guide to NumPy*, Trelgol Publishing, U.S.A., available at <http://www.numpy.org/> (last accessed March 2020).
- Otsu, N. (1979). A threshold selection method from gray-level histograms, *IEEE Trans. Syst. Man Cybern.* **9**, no. 1, 62–66.
- Pintore, S., M. Quintiliani, and D. Franceschi (2005). Teseo: A vectoriser of historical seismograms, *Comput. Geosci.* **31**, no. 10, 1277–1285.
- Poli, P., H. Hersbach, D. P. Dee, P. Berrisford, A. J. Simmons, F. Vitart, P. Laloyaux, D. G. Tan, C. Peubey, J.-N. Thépaut, *et al.* (2016). ERA-20c: An atmospheric reanalysis of the twentieth century, *J. Clim.* **29**, no. 11, 4083–4097.
- Rasche, N., and F. Arduin (2013). A global wave parameter database for geophysical applications. Part 2: Model validation with improved source term parameterization, *Ocean Model.* **70**, 174–188.
- Reguero, B. G., I. J. Losada, and F. J. Méndez (2019). A recent increase in global wave power as a consequence of oceanic warming, *Nat. Commun.*, **10**, 205, doi: [10.1038/s41467-018-08066-0](https://doi.org/10.1038/s41467-018-08066-0).
- Rew, R., and G. Davis (1990). NetCDF: An interface for scientific data access, *IEEE Comput. Graph. Appl.* **10**, no. 4, 76–82.
- Roux, P., D. Bindi, T. Boxberger, A. Colombi, F. Cotton, I. Douste-Bacque, S. Garambois, P. Gueguen, G. Hillers, D. Hollis, *et al.* (2018). Toward seismic metamaterials: The METAFORÉ project, *Seismol. Res. Lett.* **89**, no. 2A, 582–593.
- Royal Observatory of Belgium (1985). Belgian seismic network, doi: [10.7914/SN/BE](https://doi.org/10.7914/SN/BE).
- Shearer, P. M. (2019). *Introduction to Seismology*, Cambridge University Press, Cambridge, United Kingdom.
- Somville, O. (1914). Observations sismologiques faites à Uccle, en 1910, 1911, 1912 et 1913, *Technical Rept.*, The Royal Observatory of Belgium, Brussels, Belgium.
- Somville, O. (1922a). Constantes des sismographes galitzine, in *Annales de l'Observatoire Royal de Belgique*, Vol. 1, The Royal Observatory of Belgium, Brussels, Belgium (in French).
- Somville, O. (1922b). Sur la methode d'enregistrement galvanometrique appliquee aux sismographes galitzine, in *Annales de l'Observatoire Royal de Belgique*, Vol. 1, The Royal Observatory of Belgium, Brussels, Belgium (in French).
- Somville, O. (1930). Bulletin Séismique de l'Observatoire royal de Belgique, *Technical Rept.*, The Royal Observatory of Belgium, Royal Observatory of Belgium, Brussels, Belgium (in French).
- Somville, O. (1931). Bulletin Séismique de l'Observatoire royal de Belgique, *Technical Rept.*, The Royal Observatory of Belgium, Brussels, Belgium (in French).
- Somville, O. (1932). Bulletin Séismique de l'Observatoire royal de Belgique, *Technical Rept.*, The Royal Observatory of Belgium, Brussels, Belgium (in French).
- Somville, O. (1933). Bulletin Séismique de l'Observatoire royal de Belgique, *Technical Rept.*, The Royal Observatory of Belgium, Brussels, Belgium (in French).
- Somville, O. (1934). Bulletin Séismique de l'Observatoire royal de Belgique, *Technical Rept.*, The Royal Observatory of Belgium, Brussels, Belgium (in French).
- Somville, O. (1935). Bulletin Séismique de l'Observatoire royal de Belgique, *Technical Rept.*, The Royal Observatory of Belgium, Brussels, Belgium (in French).
- Somville, O. (1936). Bulletin Séismique de l'Observatoire royal de Belgique, *Technical Rept.*, The Royal Observatory of Belgium, Brussels, Belgium (in French).
- Somville, O. (1937a). Bulletin Séismique de l'Observatoire royal de Belgique, *Technical Rept.*, The Royal Observatory of Belgium, Brussels, Belgium (in French).
- Somville, O. (1937b). *Un nouveau type de sismographe vertical*, Vol. 15, Publications du Bureau central séismologique international, Fascicule, 137–145 (in French).
- Somville, O. (1953). Bulletin Séismique de l'Observatoire royal de Belgique, *Technical Rept.*, The Royal Observatory of Belgium, Brussels, Belgium (in French).
- Stopa, J. E., F. Arduin, E. Stutzmann, and T. Lecocq (2019). Sea state trends and variability: Consistency between models, altimeters, buoys, and seismic data (1979–2016), *J. Geophys. Res.* **124**, no. 6, 3923–3940.

- Stutzmann, E., F. Ardhuin, M. Schimmel, A. Mangeney, and G. Patau (2012). Modelling long-term seismic noise in various environments, *Geophys. J. Int.* **191**, no. 2, 707–722.
- Tolman, H. L., and the WAVEWATCH III Development Group (2014). User manual and system documentation of WAVEWATCH III version 4.18, *Technical Note 316*, NOAA/NWS/NCEP/MMAB.
- Van Camp, M., and T. Camelbeek (2004). Histoire des stations sismiques belges: de la station <<Solvay>> au réseau national de surveillance sismique, *Ciel et Terre* **120**, no. 6, 162–176 (in French).
- van der Walt, S., J. L. Schönberger, J. Nunez-Iglesias, F. Boulogne, J. D. Warner, N. Yager, E. Gouillart, and T. Yu (2014). Scikit-image: Image processing in Python, *PeerJ* **2**, e453.
- Van Noten, K., T. Lecocq, C. Sira, K.-G. Hinzen, and T. Camelbeek (2017). Path and site effects deduced from transfrontier internet macroseismic data of two recent M4 earthquakes in NW Europe, *Solid Earth* **8**, 453–477, doi: [10.5194/se-8-453-2017](https://doi.org/10.5194/se-8-453-2017).
- Virtanen, P., R. Gommers, T. E. Oliphant, M. Haberland, T. Reddy, D. Cournapeau, E. Burovski, P. Peterson, W. Weckesser, J. Bright, et al. (2020). SciPy 1.0: Fundamental algorithms for scientific computing in Python, *Nat. Methods* **17**, 261–272 doi: [10.1038/s41592-019-0686-2](https://doi.org/10.1038/s41592-019-0686-2).
- Wadey, M. P., I. D. Haigh, R. J. Nicholls, J. M. Brown, K. Horsburgh, B. Carroll, S. L. Gallop, T. Mason, and E. Bradshaw (2015). A comparison of the 31 January–1 February 1953 and 5–6 December 2013 coastal flood events around the UK, *Front. Mar. Sci.*, **2**, 84, doi: [10.3389/fmars.2015.00084](https://doi.org/10.3389/fmars.2015.00084).
- Wang, M., Q. Jiang, and Z. Pan (2014). A new curve tracing algorithm based on local feature in the vectorization of paper seismograms, *Sens. Transducers* **165**, no. 2, 4.
- Welch, P. (1967). The use of fast Fourier transform for the estimation of power spectra: A method based on time averaging over short, modified periodograms, *IEEE Trans. Audio Electroacoust.* **15**, no. 2, 70–73.
- Wemelsfelder, P. J. (1953). The disaster in The Netherlands caused by the storm flood of February 1, 1953, *Coast. Eng. Proc.* **1**, no. 4, 18.
- Wenner, F., and H. E. McComb (1936). The Galitzin seismometer: Discrepancies between the Galitzin theory and the performance of a Wilip-Galitzin seismometer, *Bull. Seismol. Soc. Am.* **26**, no. 4, 317–322.
- Whitaker, J., C. Khrulev, D. Huard, C. Paulik, F. Stephan Hoyer, L. Pastewka, A. Mohr, C. Marquardt, B. Couwenberg, J. Whitaker, et al. (2019). Unidata/netcdf4-python: version 1.5.1.2 release, available at <https://zenodo.org/record/2669496#.XSR6GIgzZjE> (last accessed March 2020).
- Wolf, J., and R. A. Flather (2005). Modelling waves and surges during the 1953 storm, *Phil. Trans. Roy. Soc. Lond. A* **363**, no. 1831, 1359–1375.

Manuscript received 26 September 2019

Published online 1 April 2020